

# Removal of a dense bottom layer by a gravity current

Rui Zhu<sup>1,2</sup>, Zhiguo He<sup>1,†</sup> and Eckart Meiburg<sup>2,†</sup>

<sup>1</sup>Ocean College, Zhejiang University, Zhoushan 316021, PR China

<sup>2</sup>Department of Mechanical Engineering, University of California at Santa Barbara, Santa Barbara, CA 93106, USA

(Received 13 July 2020; revised 19 January 2021; accepted 9 March 2021)

We investigate the removal of a dense bottom layer by a gravity current, via Navier–Stokes simulations in the Boussinesq limit. The problem is governed by a dimensionless thickness parameter for the bottom layer, and by the ratio of the density differences between bottom layer, gravity current and ambient fluids. A quasisteady gravity current forms that propagates along the interface and displaces some of the dense bottom fluid, which accumulates ahead of the gravity current and forms an undular bore or a series of internal gravity waves. Depending on the ratio of the gravity current front velocity to the linear shallow-water wave velocity, we observe the existence of different regimes, characterized by small-amplitude waves or by a train of steep, nonlinear internal waves. We develop a semiempirical model that provides reasonable estimates of several important flow properties. We also formulate a more sophisticated, self-contained model based on the conservation principles for mass and vorticity that does not require empirical closure assumptions. This model is able to predict such quantities as the gravity current height and the internal wave or bore velocity as a function of the governing dimensionless parameters, generally to within approximately a 10 % accuracy. An energy budget analysis provides information on the rates at which potential energy is converted into kinetic energy and then dissipated, and on the processes by which energy is transferred from the gravity current fluid to the dense and ambient fluids. We observe that the energy content of thicker and denser bottom layers grows more rapidly.

**Key words:** gravity currents, internal waves, stratified flows

## 1. Introduction

Density-driven, predominantly horizontal flows in the form of gravity currents play a central role in a host of natural processes, as well as in numerous engineering applications

† Email addresses for correspondence: [hezhi guo@zju.edu.cn](mailto:hezhi guo@zju.edu.cn), [meiburg@engineering.ucsb.edu](mailto:meiburg@engineering.ucsb.edu)

© The Author(s), 2021. Published by Cambridge University Press. This is an Open Access article, distributed under the terms of the Creative Commons Attribution licence (<http://creativecommons.org/licenses/by/4.0/>), which permits unrestricted re-use, distribution, and reproduction in any medium, provided the original work is properly cited.

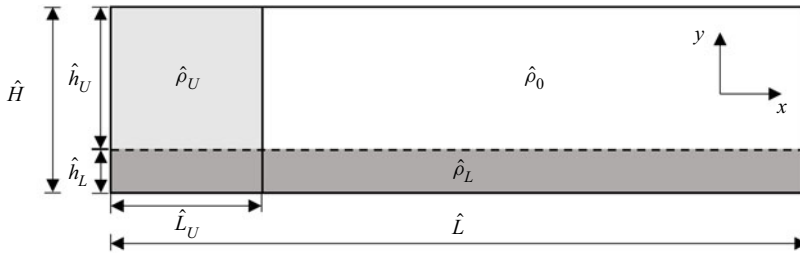


Figure 1. The initial set-up: above a dense layer of uniform thickness that covers the bottom of the entire tank, intermediate density fluid is placed in the left-hand compartment, while light fluid fills the right-hand compartment. At time  $t = 0$  the gate separating the two compartments is removed, so that a gravity current forms that propagates to the right while interacting with the dense fluid layer.

(Simpson 1982). The interaction of such gravity currents with a dense bottom layer can give rise to rich and complex dynamics (Samothrakis & Cotel 2006a,b; Monaghan 2007; He *et al.* 2017, 2019; Ouillon *et al.* 2019a; Ouillon, Meiburg & Sutherland 2019b; Tanimoto, Ouellette & Koseff 2020). An interesting example in this regard concerns the sundowner winds near Santa Barbara, California, which propagate down the southern slope of the Santa Ynez Mountains. When they encounter the denser marine atmospheric boundary layer above the ocean, they can trigger internal gravity waves at the top of this layer (Smith, Hatchett & Kaplan 2018; Carvalho 2020). Similar processes may occur in estuaries when river outflows interact with a dense bottom layer near the seafloor, or in the context of effluents from desalination plants (Lattemann & Amy 2013). For example, near the southern end of the Dead Sea such a dense bottom layer has been observed to form as a result of the very salty discharge from a desalination plant, and the question arises as to whether gravity currents might be able to remove or dilute this dense bottom layer.

The majority of the above studies have focused on situations in which a gravity current travelling down an inclined slope encounters a stably stratified interface. Depending on the slope angle, the relative densities of the gravity current and the ambient fluid layers, the interaction between the current and the interface can result in the formation of an intrusion and/or a dense underflow, and it can trigger the emergence of internal gravity waves. By contrast, the present investigation aims to shed light on how a gravity current can trigger interfacial waves and bores in the situation where the bottom boundary is horizontal, and how a dense bottom layer can be removed by means of a gravity current. Towards this end we focus on the model problem sketched in figure 1. We consider a two-dimensional (2-D) tank of length  $\hat{L}$  and height  $\hat{H}$ . Initially, the bottom of the entire tank is occupied by a shallow, dense fluid layer of depth  $\hat{h}_L$  and density  $\hat{\rho}_L$ . Above this dense bottom layer, the left-hand section of length  $\hat{L}_U$  and height  $\hat{h}_U$  is filled entirely with fluid of intermediate density  $\hat{\rho}_U$ , while the right-hand section holds ambient light fluid of density  $\hat{\rho}_0$ . At time  $\hat{t} = 0$  we remove the gate that separates the light fluid from the intermediate density fluid, so that a right-propagating gravity current forms on top of the dense bottom layer. As the density interface is deformed by this advancing gravity current, it will give rise to interfacial perturbations whose propagation velocity may or may not exceed the front velocity of the gravity current, so that we expect different flow regimes to emerge as the ratio of these velocities varies. We remark that the present study focuses on full-depth lock release flows only, and that  $\hat{L}_U$  was chosen sufficiently large so that its precise value does not have a strong effect on the results.

We note that the situation sketched in [figure 1](#) differs in several key aspects from the one in which all of the fluid initially to the left of the gate is of the same intermediate density, so that a dense bottom layer exists only to the right of the gate. This set-up has been explored in some detail, going back to the early experimental investigations by Holyer & Huppert (1980) and Britter & Simpson (1981), and it can exhibit interesting symmetry properties. The so-called doubly symmetric configuration is obtained when the ambient layers have equal depths and the density of the fluid to the left of the gate is the average of the ambient densities. Even when the ambient fluid layers are unequal in depth, a certain dynamic symmetry holds as long as the density of the lock fluid corresponds to the depth-weighted mean density of the two ambient layers (Sutherland, Kyba & Flynn 2004). When this condition is satisfied, the interface ahead of the intrusion remains flat, whereas otherwise a leading waveforms. The effect of small deviations from this symmetric configuration can be captured by a perturbation analysis (Sutherland *et al.* 2004). Various aspects of this flow configuration, such as front velocity, velocity structure and wave excitation were further analysed by Cheong, Kuenen & Linden (2006), Flynn & Linden (2006), Lowe, Linden & Rottman (2002), Mehta, Sutherland & Kyba (2002) and Ooi, Constantinescu & Weber (2007), as well as by De Rooij, Linden & Dalziel (1999), who focused on the dynamics of a corresponding particle-laden flow. Khodkar, Nasr-Azadani & Meiburg (2016) proposed theoretical models for both the symmetric and non-symmetric variants of such flows, based on the conservation principles of mass and vorticity. This approach, which does not require closure assumptions for the pressure variable, reproduces the experimentally observed symmetry properties, and it yields good quantitative agreement regarding various properties of the evolving flow field. We remark that, by its very nature, the configuration sketched in [figure 1](#) with a dense fluid layer also to the left of the gate cannot give rise to corresponding geometric or dynamical flow symmetries, since it does not produce a left-propagating countercurrent along the bottom wall. Hence it represents an interesting subject of exploration in its own right.

This paper is organized as follows. Section 2 describes the computational model, including the governing equations, initial and boundary conditions and the numerical approach. In §3, we analyse the dynamic behaviour of the gravity current and the dense bottom fluid layer in detail, to demonstrate the existence of different flow regimes. Based on numerical observations, we develop a semiempirical model that is able to reproduce several of the flow features quantitatively. Subsequently, we propose a more comprehensive vorticity-based model that does not require any empirical closure assumptions. Furthermore, we analyse the conversion of potential to kinetic energy in some detail, along with the energy transfer among the different fluids. Finally, §4 summarizes our findings and presents the main conclusions.

## 2. Computational model

### 2.1. Governing equations

We assume that all density variations are due to different concentrations of the same scalar, which we will refer to as ‘salinity’ in the following. After invoking the Boussinesq approximation, the dimensional governing equations for the conservation of mass, momentum and concentration take the form

$$\frac{\partial \hat{u}_j}{\partial \hat{x}_j} = 0, \quad (2.1)$$

$$\frac{\partial \hat{u}_i}{\partial \hat{t}} + \hat{u}_j \frac{\partial \hat{u}_i}{\partial \hat{x}_j} = -\frac{1}{\hat{\rho}_0} \frac{\partial \hat{p}}{\partial \hat{x}_i} + \hat{\nu} \frac{\partial^2 \hat{u}_i}{\partial \hat{x}_j \partial \hat{x}_j} + \frac{\hat{\rho} - \hat{\rho}_0}{\hat{\rho}_0} \hat{g} e_i^g, \quad (2.2)$$

$$\frac{\partial \hat{s}_U}{\partial \hat{t}} + \hat{u}_j \frac{\partial \hat{s}_U}{\partial \hat{x}_j} = \hat{\kappa}_s \frac{\partial^2 \hat{s}_U}{\partial \hat{x}_j \partial \hat{x}_j}, \quad (2.3)$$

$$\frac{\partial \hat{s}_L}{\partial \hat{t}} + \hat{u}_j \frac{\partial \hat{s}_L}{\partial \hat{x}_j} = \hat{\kappa}_s \frac{\partial^2 \hat{s}_L}{\partial \hat{x}_j \partial \hat{x}_j}. \quad (2.4)$$

Here  $\hat{u}$  denotes the fluid velocity, with the subscripts  $i, j$  indicating the  $x$ - and  $y$ -direction, respectively. The upper boundary of the dense fluid layer is located at  $y = 0$ . Here  $\hat{t}$  represents time,  $\hat{\rho}$  the local density,  $\hat{\nu}$  the kinematic viscosity and  $\hat{\kappa}_s$  the diffusivity of salt. The gravitational acceleration  $\hat{g}$  points in the direction of the unit normal vector  $e_i^g = (0, -1)$ . The salinity values of the upper-layer lock fluid and the bottom layer are denoted by  $\hat{s}_U$  and  $\hat{s}_L$ , respectively. By keeping track of these separately, we are able to obtain more detailed information on the Lagrangian motion of the different initial fluid regions, for example on the interface between the current and the dense layer, about their mixing behaviour, and regarding the exchange of energy between the gravity current and the dense layer fluids, with minimal additional computational expense.

We assume a linear density–salinity relationship with the expansion coefficient  $\beta$

$$\hat{\rho} = \hat{\rho}_0 + \beta(\hat{s}_U + \hat{s}_L), \quad (2.5)$$

so that for the initial salinity values  $\hat{s}_{U,init}$  and  $\hat{s}_{L,init}$  we obtain

$$\hat{\rho}_U = \hat{\rho}_0 + \beta \hat{s}_{U,init}, \quad (2.6)$$

$$\hat{\rho}_L = \hat{\rho}_0 + \beta \hat{s}_{L,init}. \quad (2.7)$$

We non-dimensionalize the governing equations by introducing characteristic scales of the form

$$x = \frac{2\hat{x}}{\hat{h}_U}, \quad u = \frac{\hat{u}}{\hat{u}_b}, \quad t = \frac{2\hat{t}\hat{u}_b}{\hat{h}_U}, \quad p = \frac{\hat{p}}{\hat{\rho}_0 \hat{u}_b^2}, \quad s_U = \frac{\hat{s}_U}{\hat{s}_{U,init}}, \quad s_L = \frac{\hat{s}_L}{\hat{s}_{L,init}}, \quad (2.8a-f)$$

where  $\hat{u}_b = \sqrt{\hat{g}\hat{h}_U(\hat{\rho}_U - \hat{\rho}_0)/2\hat{\rho}_0}$  indicates the buoyancy velocity. In this way, we arrive at the non-dimensional equations

$$\frac{\partial u_j}{\partial x_j} = 0, \quad (2.9)$$

$$\frac{\partial u_i}{\partial t} + u_j \frac{\partial u_i}{\partial x_j} = -\frac{\partial p}{\partial x_i} + \frac{1}{Re} \frac{\partial^2 u_i}{\partial x_j \partial x_j} + (s_U + R_{LSL}) e_i^g, \quad (2.10)$$

$$\frac{\partial s_U}{\partial t} + u_j \frac{\partial s_U}{\partial x_j} = \frac{1}{Pe} \frac{\partial^2 s_U}{\partial x_j \partial x_j}, \quad (2.11)$$

$$\frac{\partial s_L}{\partial t} + u_j \frac{\partial s_L}{\partial x_j} = \frac{1}{Pe} \frac{\partial^2 s_L}{\partial x_j \partial x_j}. \quad (2.12)$$

As governing dimensionless parameters, we obtain the Reynolds number,  $Re$ ,

$$Re = \frac{\hat{u}_b \hat{h}_U}{2\hat{\nu}}, \quad (2.13)$$

Run	1	2	3	4	5	6	7	8	9	10	11	12	13
$h_L$	0.2	0.2	0.2	0.2	0.4	0.4	0.4	0.6	0.6	0.6	0.0	0.1	0.1
$Re$	7301	7301	7301	7301	7301	7301	7301	7301	7301	7301	7301	7301	7301
$R_L$	1.00	1.43	2.00	5.00	1.43	2.00	5.00	1.43	2.00	5.00	0.00	1.43	2.00

Table 1. Overview of the simulations conducted and the associated parameter values.

the Péclet number,  $Pe$ ,

$$Pe = \frac{\hat{u}_b \hat{h}_U}{2\hat{\kappa}_s}, \quad (2.14)$$

the density parameter,  $R_L$ ,

$$R_L = \frac{\hat{\rho}_L - \hat{\rho}_0}{\hat{\rho}_U - \hat{\rho}_0}, \quad (2.15)$$

where  $Re$  and  $Pe$  are related by the Schmidt number  $Sc$  as follows:

$$Sc = \frac{Pe}{Re} = \frac{\hat{\nu}}{\hat{\kappa}_s}. \quad (2.16)$$

In the following we set  $Sc = 1$ , based on observations by earlier authors who found that for similar flows the value of  $Sc$  has a negligible effect, as long as it is at least unity (Necker *et al.* 2005). The evolving gravity current is thus fully characterized by  $Re$ ,  $R_L$  and the dimensionless thickness  $h_L$  of the bottom fluid layer. In the following, we will focus on the influence of  $R_L$  and  $h_L$ , by discussing simulation results for sufficiently high Reynolds numbers so that the precise value of  $Re$  is of minor importance.

## 2.2. Initial and boundary conditions

Unless otherwise noted, the tank extends over  $L = 80$ , with a lock length  $L_U = 10$ . No-slip conditions are enforced along the bottom and sidewalls, while the upper boundary is modelled as a free surface by implementing a non-deformable slip wall. The salinity field is subject to no-flux conditions along all boundaries. Initially, the fluid is at rest everywhere. We will discuss results from a total of 13 simulations, whose parameters are listed in [table 1](#).

## 2.3. Numerical method

All simulations are conducted with our in-house incompressible Navier–Stokes solver PARTIES, which employs second-order central finite differences to discretize the viscous and diffusive terms, along with a second-order upwind scheme for the advection terms (Biegert, Vowinckel & Meiburg 2017a; Biegert *et al.* 2017b). Time integration is performed by means of a third-order low-storage Runge–Kutta method. The pressure-projection method is implemented, based on a direct fast Fourier transform solver for the resulting Poisson equation at each Runge–Kutta substep. Validation results presented by Nasr-Azadani & Meiburg (2011) and Nasr-Azadani, Hall & Meiburg (2013)

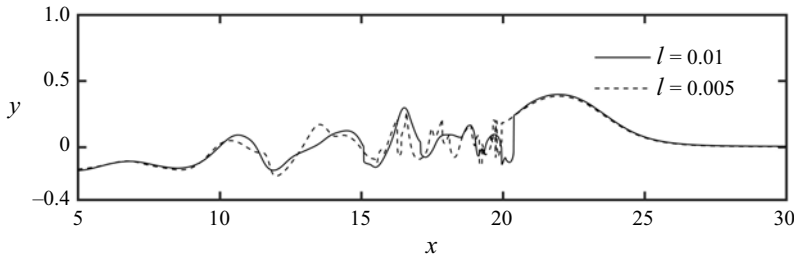


Figure 2. The interfacial waveforms for run 6 for different grid spacings at  $t = 15$ , as obtained from the shape of the contour  $s_L = 0.5$ . The close agreement between the two lines indicates that the simulations are converged.

indicate that the uniform mesh size  $l$  should satisfy

$$l < \frac{1}{\sqrt{ReSc}}. \tag{2.17}$$

Accordingly, we employ  $l = 0.01$  in all simulations. To demonstrate convergence of the numerical results, we simulated run 6 also for a finer grid with  $l = 0.005$ . The interfacial shape is shown in figure 2 by means of the contour  $s_L = 0.5$  at  $t = 15$ . Ahead of and behind the gravity current, the interfacial waveforms of the two simulations are in close agreement, which indicates that the results are converged. On the other hand, the chaotic, vortical nature of the flow near the interfacial region between the bottom layer and the gravity current prevents a similarly close agreement in this region, or a strict power-law convergence of the interfacial shapes. Nevertheless, moving average values for the interface locations in this region are very close.

#### 2.4. Two-dimensional versus three-dimensional simulations

In order to assess the importance of three-dimensional (3-D) effects, we ran a 3-D simulation for the same parameters as run 6. The width of the computational domain in the spanwise  $z$ -direction was 2.4. Figure 3 compares the dimensionless density fields at various times for the 2-D case (panels (a), (c) and (e)) with the spanwise average for the 3-D simulation (panels (b), (d) and (f)). The flow at early times ( $t = 5$ ) after the release is similar for the 2-D and 3-D simulations. During the later stages ( $t = 20$  and 40), the Kelvin–Helmholtz vortices are more pronounced in the 2-D simulation than in three dimensions. However, such quantities as the front location and the terms in the energy equation, shown in figure 4, are essentially identical in two and three dimensions. Details regarding the front location and energy terms will be discussed in §§ 3.1 and 3.5, respectively. Hence we conclude that the addition of the third dimension in the simulations has only a weak effect on those key features that are the focus of the present investigation.

### 3. Results

#### 3.1. Flow regimes

The density fields shown in figure 5 illustrate some of the flow patterns that can emerge for different values of the density parameter  $R_L$ , if the lower layer thickness is held at a constant value  $h_L = 0.2$ . For the densest bottom layer with  $R_L = 5$ , we observe the formation of a small-amplitude undular bore at the interface between the upper and lower layers that propagates significantly faster than the gravity current front. The amplitudes of

## Removal of a dense bottom layer by a gravity current

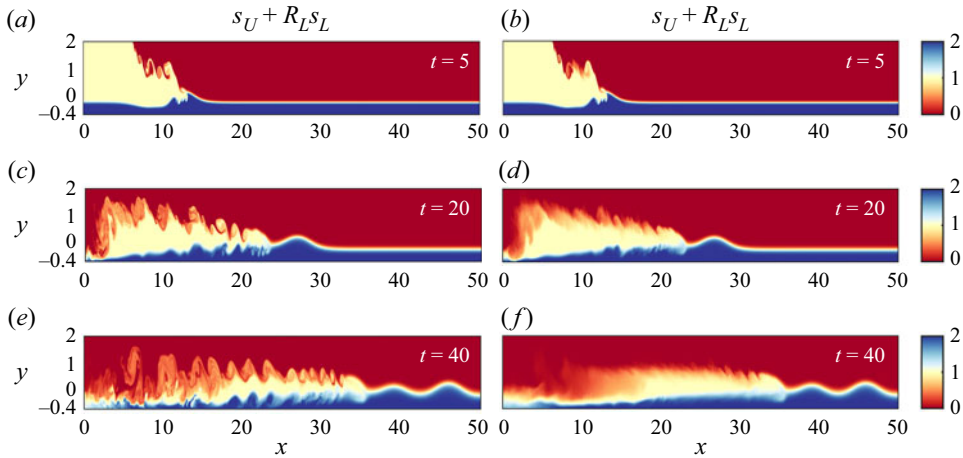


Figure 3. Dimensionless density fields for 2-D and 3-D simulations with  $R_L = 2$  and  $h_L = 0.4$ ; panels (a), (c) and (e) show the 2-D results at  $t = 5, 20$  and  $40$ ; panels (b), (d) and (f) show the corresponding 3-D results at the same times. While the Kelvin–Helmholtz vortices are more pronounced in the 2-D simulation, the shapes of the undular bores are nearly identical in two and three dimensions.

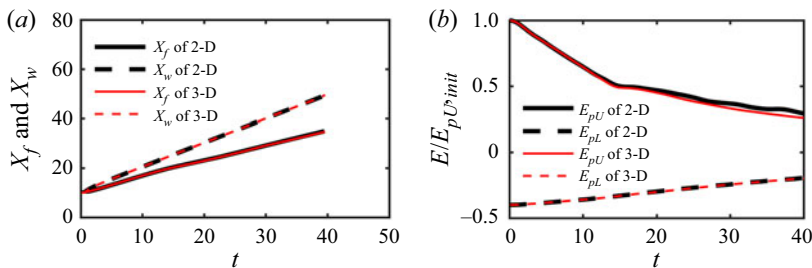


Figure 4. Time history of the front location and energy budget terms for the 2-D and 3-D simulations with  $R_L = 2$  and  $h_L = 0.4$ : (a) front position of the gravity current  $X_f$  and location of the wave  $X_w$ ; (b) potential energy of the gravity current  $E_{pU}$  and dense layer fluid  $E_{pL}$ . The 2-D and 3-D results show close agreement.

the wave crests that follow the bore front remain much smaller than the gravity current height throughout the simulation.

For the intermediate density bottom layer with  $R_L = 2$ , the perturbation evolving along the interface between the lower and upper layers propagates significantly more slowly, although still faster than the gravity current front. Rather than an undular bore, we observe a train of distinct nonlinear individual waves whose amplitude is comparable to the gravity current height. The front velocity of the gravity current remains similar to that of the  $R_L = 5$  case, as shown in [figure 6](#).

Finally, for  $R_L = 1.43$  the perturbation along the interface between the upper and lower fluid layers slows down even further, although the gravity current velocity remains essentially unchanged. A significant amount of gravity current fluid becomes entrained into the emerging large-amplitude interfacial wave, before this wave separates from the gravity current front and propagates a short distance ahead of it. Furthermore, we note that shear-generated Kelvin–Helmholtz waves evolve along the interfaces between the gravity current and the ambient, and the gravity current and the dense bottom layer.

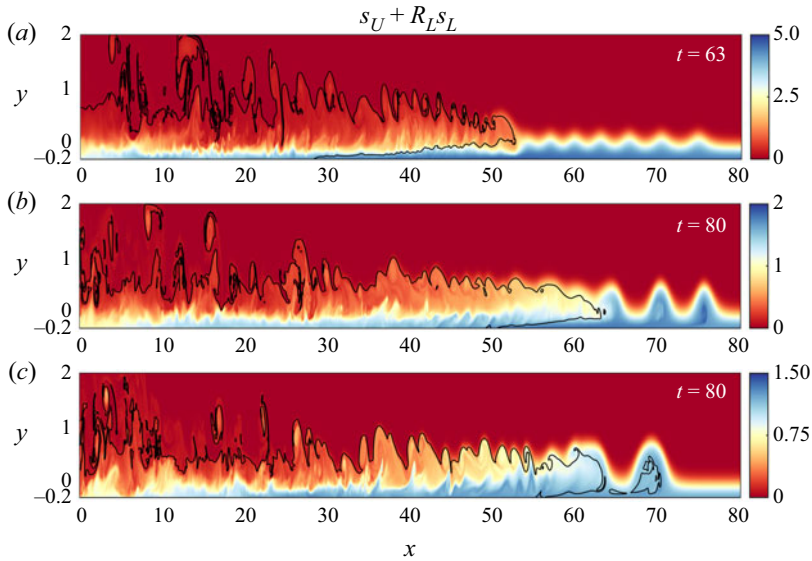


Figure 5. Dimensionless density fields for a constant lower layer thickness  $h_L = 0.2$ , and different values of the density ratio  $R_L$ : (a) run 4 with  $R_L = 5$ ; (b) run 3 with  $R_L = 2$ ; (c) run 2 with  $R_L = 1.43$ . For smaller density contrasts the interfacial waves propagate more slowly, and they increase in amplitude. The black contour represents the value  $s_U = 0.1$ .

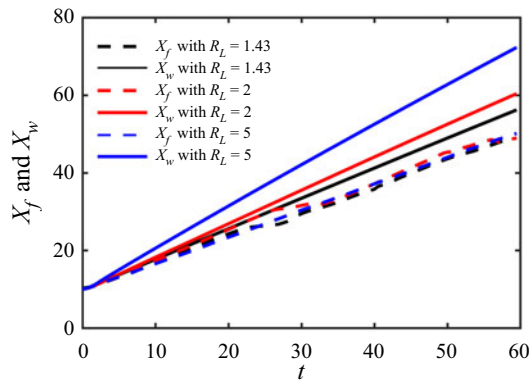


Figure 6. Position  $X_f$  of the gravity current front (dashed lines) and location  $X_w$  of the leading interfacial wave (solid lines) for the flows shown in figure 5, as functions of time. The density ratio  $R_L$  has a strong influence on the interfacial wave velocity, whereas its effect on the gravity current velocity is small.

Figure 6 shows the front locations of the gravity currents,  $X_f$ , and of the bore or internal waves,  $X_w$ , as functions of time. Here, we define the gravity current front as the rightmost location in the flow field with  $s_U > 0.2$ , which excludes the gravity current fluid entrained into the waves in runs 2 and 3 from being considered. The front of the bore or internal wave is evaluated as the foremost point above  $y = 0.1$  with  $s_L = 0.5$ . The graph indicates that the bore or internal waves move with approximately constant velocity, while the gravity current velocity varies somewhat with time. Larger values of  $R_L$  result in faster interfacial waves, but they do not alter the gravity current velocity appreciably.

Figure 7 shows the corresponding density fields for simulations with a constant density ratio  $R_L = 1.43$  and different bottom layer thicknesses  $h_L$ . For the thickest lower layer with



## Removal of a dense bottom layer by a gravity current

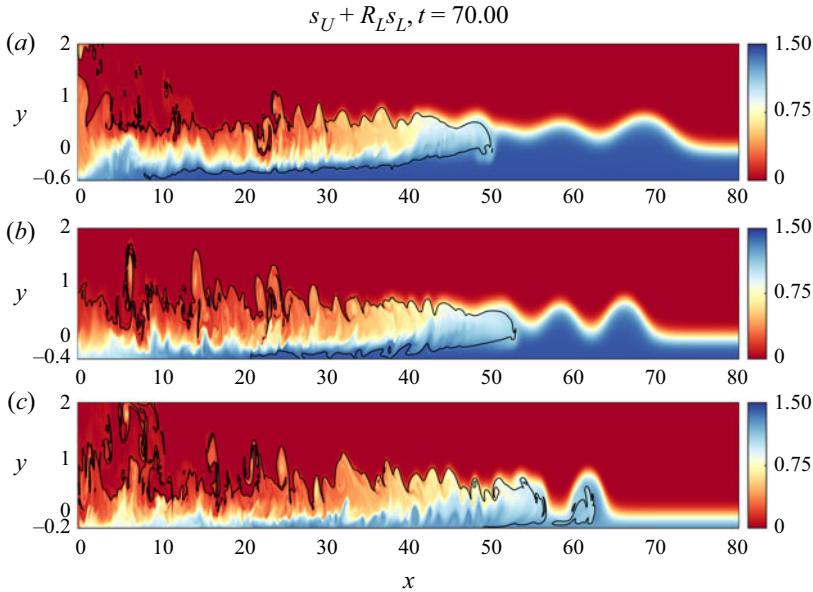


Figure 7. Dimensionless density fields for a constant density ratio  $R_L = 1.43$ , and different values of the layer thickness  $h_L$ : (a) run 8 with  $h_L = 0.6$ ; (b) run 5 with  $h_L = 0.4$ ; (c) run 2 with  $h_L = 0.2$ . For thinner bottom layers the interfacial waves propagate more slowly, and they increase in amplitude. The black contour represents the value  $s_U = 0.1$ .

$h_L = 0.6$  an undular bore forms at the interface. The relatively long waves following the bore exhibit comparatively small amplitudes. For the intermediate lower layer thickness of  $h_L = 0.4$ , the waves propagate more slowly, their amplitude increases, and their wavelength is reduced. This trend is even more pronounced in the thinnest lower layer with  $h_L = 0.2$ .

In order to arrive at quantitative descriptions of these qualitatively different flow fields, we now proceed to analyse the dependence of the bore, internal wave and gravity current velocities on  $R_L$  and  $h_L$ .

### 3.2. Gravity current, undular bore and internal wave velocities

Several analytical models exist for predicting the front velocity of inviscid gravity currents propagating over a solid wall. In his classical analysis, Benjamin (1968) obtains the dimensionless front velocity as

$$U_{f,B} = \frac{\hat{U}_{f,B}}{\hat{u}_b} = \sqrt{\frac{2\alpha(1-\alpha)(2-\alpha)}{\sigma(1+\alpha)}}, \quad (3.1)$$

where  $\sigma = \hat{\rho}_0/\hat{\rho}_U$  and  $\alpha = \hat{h}_{gc}/\hat{h}_U$ , with  $\hat{h}_{gc}$  denoting the gravity current height and  $\hat{h}_U$  the initial height of the gravity current fluid in the lock. By focusing on the conservation of vorticity, Borden & Meiburg (2013a) derive a corresponding dimensionless result for Boussinesq currents in the form

$$U_{f,BM} = \frac{\hat{U}_{f,BM}}{\hat{u}_b} = 2\sqrt{\alpha}(1-\alpha). \quad (3.2)$$

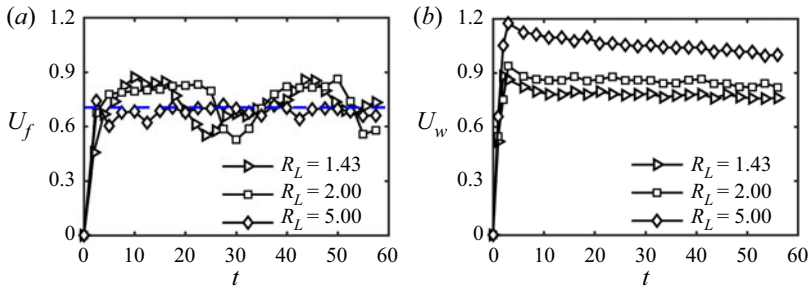


Figure 8. (a) The gravity current front velocity  $U_f$  for runs 2, 3 and 4 as a function of time. The dashed blue line represents the predicted velocity of  $1/\sqrt{2}$  for half-depth currents. The average front velocity for all three gravity currents is close to this value, which suggests that the gravity currents behave approximately as half-depth currents. (b) The undular bore or leading internal wave velocity  $U_w$  for runs 2, 3 and 4 as a function of time.

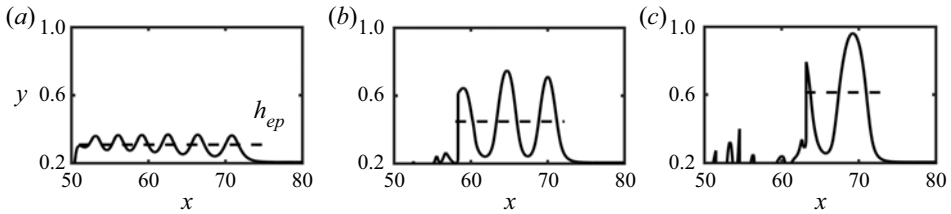


Figure 9. The waveforms of the bore and internal waves, as obtained from the shape of the contour  $s_L = 0.5$ : (a) run 4 with  $R_L = 5$  and  $h_L = 0.2$  at  $t = 59$ ; (b) run 3 with  $R_L = 2$  and  $h_L = 0.2$  at  $t = 73$ ; (c) run 2, with  $R_L = 1.43$  and  $h_L = 0.2$  at  $t = 80$ . The dotted lines indicate the respective equilibrium heights  $h_{ep}$ , which are obtained by averaging the layer thickness between the first and last peak.

For a Boussinesq gravity current with height equal to half the upper fluid layer thickness, so that  $\sigma = 1$  and  $\alpha = 1/2$ , both of these relationships predict a dimensionless front velocity of  $1/\sqrt{2} \approx 0.71$ . Figure 8(a) indicates that this value provides a reasonably good estimate of the computationally observed, fluctuating gravity current front velocities for runs 2, 3 and 4, which suggests that these gravity currents behave approximately as half-depth currents.

Figure 8(b) shows the velocity  $U_w$  of the bore or internal waves as a function of time, again for runs 2, 3 and 4. After an initial acceleration phase a quasisteady state emerges that is characterized by an approximately constant wave speed. In order to quantify this quasisteady bore or wave velocity, we refer to the circulation model of Borden & Meiburg (2013b), which predicts the propagation velocity of an inviscid bore advancing over a solid wall as

$$U_{w,BM} = \frac{\hat{U}_{w,BM}}{\hat{u}_b} = \sqrt{\frac{2R_L h_L}{h_U}} \sqrt{\frac{2R^2(Rr - 1)^2}{R - 2Rr + 1}}. \quad (3.3)$$

Here  $r = \hat{h}_L / (\hat{h}_L + \hat{h}_U)$  and  $R = \hat{h}_{ep} / \hat{h}_L$ , where  $\hat{h}_{ep}$  denotes the lower layer thickness behind the bore. For the flows shown in figure 5, which have undular bores or internal waves, we do not have a constant lower fluid layer thickness behind the bore, so that we define an effective equilibrium layer thickness  $\hat{h}_{ep}$  instead. This is accomplished by taking the average height of the wavy salinity contour  $s_L = 0.5$  between the first and the last peak, as indicated in figure 9 for runs 2, 3 and 4.

## Removal of a dense bottom layer by a gravity current

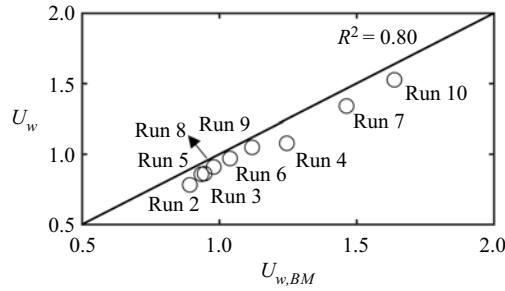


Figure 10. Comparison of the bore/internal wave propagation velocity  $U_w$  from the simulations with the value  $U_{w,BM}$  predicted by the circulation-based model of Borden & Meiburg (2013b).

We remark that in the limit of small bore amplitudes,  $R = 1$ , the bore velocity obtained from (3.3) takes the form

$$U_{w,BM}^{lim} = \sqrt{\frac{2R_L h_L}{h_U}} \sqrt{1-r} = \sqrt{\frac{2R_L h_L}{H}}, \quad (3.4)$$

which recovers the dimensionless propagation velocity of linear shallow-water waves (Kundu & Cohen 2001)

$$C_0 = \frac{\hat{C}_0}{\hat{u}_b} = \sqrt{\frac{\hat{g}(\hat{\rho}_L - \hat{\rho}_0)\hat{h}_U\hat{h}_L}{\hat{\rho}_0\hat{H}\hat{u}_b^2}} = \sqrt{\frac{2h_LR_L}{H}}. \quad (3.5)$$

Figure 10 compares the value of the front velocity  $U_w$  from the simulation with the value  $U_{w,BM}$  predicted by the model of Borden & Meiburg (2013b), for all flows that exhibit a bore or a train of waves. We find that the propagation velocities observed in the simulations are close to, although generally approximately 5%–10% below the values predicted by the model, likely because the model neglects the effects of viscosity. It is interesting to note that the velocity of the train of large-amplitude, distinct internal waves in runs 2 and 3 is predicted quite well by treating this wave train as an equivalent bore whose height equals the average height of the wave train.

### 3.3. Effective bore height

The above results suggest that the gravity current behaves approximately as a half-depth current with  $h_{gc} = 1$ , and they indicate that the circulation-based model of Borden & Meiburg (2013b) yields a good estimate of the bore velocity as a function of the effective bore height  $h_{ep}$ . In order to obtain a closed, predictive model of the evolving flow field without any adjustable constants, we still require knowledge of this effective bore height as a function of  $R_L$  and  $h_L$ . In order to obtain this relationship, we focus on the detailed formation process of the undular bore and the accompanying internal waves as shown in figure 11, for the representative flow of run 6. Upon removal of the gate, the evolving gravity current erodes some of the dense fluid at the bottom of the tank, which then accumulates ahead of the gravity current front. The front pushes this dense lower layer fluid towards the right-hand side, so that it forms a bore that propagates faster than the current front itself. As this bore separates from the gravity current front, a series of internal waves form in its wake.

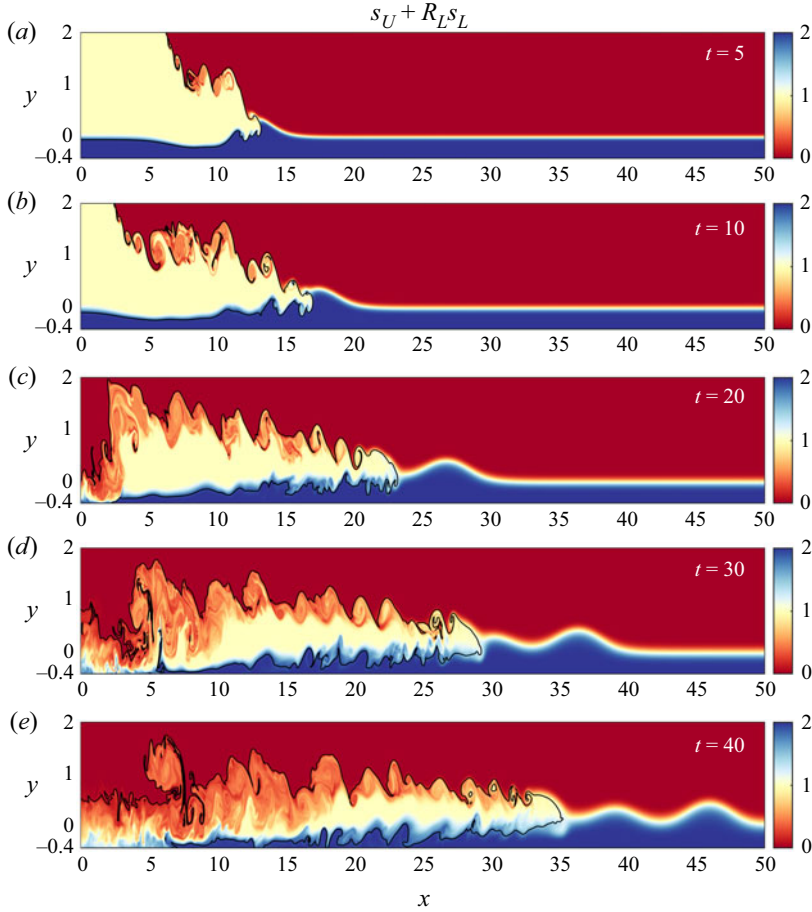


Figure 11. Details of the undular bore formation process for run 6, with  $R_L = 2$  and  $h_L = 0.4$ . Shown is the dimensionless density field at various times, along with the  $s_U = 0.1$  contour. The gravity current erodes part of the bottom layer of dense fluid, which accumulates ahead of the current front and produces an undular bore that propagates more rapidly than the gravity current itself.

A prediction of the effective bore height  $h_{ep}$  as a function of  $R_L$  and  $h_L$  can be obtained from the simplified flow model sketched in figure 12. Towards this end, we hypothesize that the depth to which the current penetrates into the lower layer is dictated by the condition that the hydrostatic pressures  $p_1 = p_2$ , which yields

$$h_1 R_L + h_{gc} = h_{ep} R_L. \quad (3.6)$$

With the earlier observation that  $h_{gc} \approx 1$ , we thus obtain

$$h_{ep} - h_1 = \frac{1}{R_L}. \quad (3.7)$$

The volumetric rate at which the gravity current erodes the dense fluid layer is  $U_f(h_{ep} - h_1) = U_f/R_L$ , so that the mass balance for the elevated interfacial region between the gravity current front and the bore yields

$$\frac{U_f}{R_L} = U_w(h_{ep} - h_L). \quad (3.8)$$

### Removal of a dense bottom layer by a gravity current

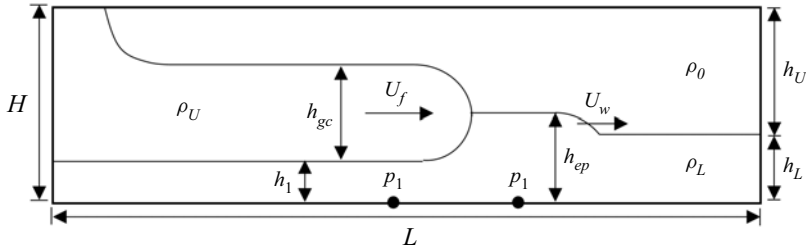


Figure 12. Simplified model for estimating the equilibrium depth  $h_{ep}$  of the dense fluid layer behind the bore, based on the assumptions that  $h_{gc} \approx 1$  and that the hydrostatic pressures  $p_1$  and  $p_2$  are in balance.

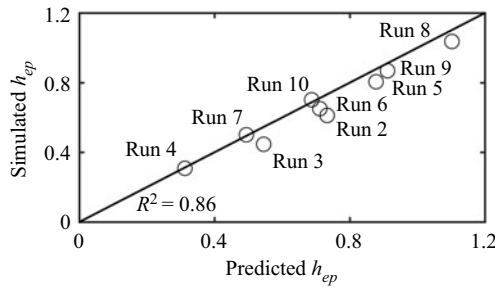


Figure 13. Comparison of the simulation values for the equilibrium layer height  $h_{ep}$  behind the bore, and the corresponding values predicted from (3.9).

Keeping in mind that  $h_{gc} \approx 1$ , we have  $U_f \approx 1/\sqrt{2}$ . Along with (3.3), we substitute this into (3.8) to obtain

$$\frac{1}{4R_L^3} = \frac{h_{ep}^2(h_{ep} - h_L)^2[h_{ep}h_L - h_L(h_L + 2)]^2}{h_L^2(h_L + 2)[(h_{ep} + h_L)(h_L + 2) - 2h_{ep}h_L]}, \quad (3.9)$$

which predicts  $h_{ep}$  implicitly as a function of  $R_L$  and  $h_L$ . Figure 13 indicates that the values of  $h_{ep}$  predicted by (3.9) agree reasonably well with the values observed in the simulations, as reflected by the coefficient of determination ('goodness of the fit'),  $R^2 = 0.86$ .

#### 3.3.1. Ratio of gravity current to linear wave velocity

Sutherland *et al.* (2004) draw attention to the important role played by the ratio of the gravity current front velocity to the propagation velocity of linear waves along the interface between the ambient and the lower layer fluids. Their experiments show that the small-amplitude linear waves observed forming for subcritical gravity currents transition to large-amplitude solitary waves when the gravity current propagates at supercritical speeds. We will now discuss the influence of this ratio for the present flow configuration.

Figure 14 shows the linear wave velocity  $C_0$  as a function of  $\sqrt{h_L R_L / H}$ , along with the velocity  $U_{f,B} = 1/\sqrt{2}$  of half-depth gravity currents predicted by Benjamin (1968) and Borden & Meiburg (2013a). The two velocities are equal for  $\sqrt{h_L R_L / H} = 1/2$ . When  $\sqrt{h_L R_L / H} > 1/2$ , small interfacial waves propagate away from the gravity current front, and a large-amplitude bore does not form. This holds for runs 4 and 6–10. For  $\sqrt{h_L R_L / H} < 1/2$ , on the other hand, small waves cannot outrun the gravity current. Hence a larger undular bore or a train of high-amplitude waves emerges whose propagation velocity  $U_w$  exceeds that of linear waves, as can be seen for runs 2, 3, 5, 12 and 13.

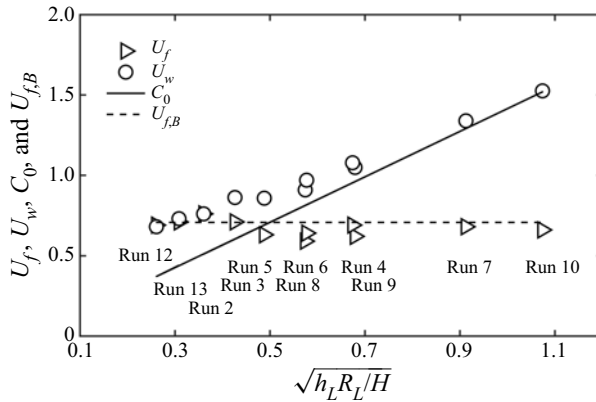


Figure 14. Gravity current velocity  $U_f$  and bore velocity  $U_w$  observed in the simulations, as functions of  $\sqrt{h_L R_L / H}$ . Also shown are the linear shallow-water wave velocity  $C_0$  and the predicted half-depth gravity current front velocity  $U_{f,B} = 1/\sqrt{2}$ . For  $C_0 > 1/\sqrt{2}$  a small-amplitude bore forms that outruns the gravity current, whereas for  $C_0 < 1/\sqrt{2}$  we observe large-amplitude waves that propagate at roughly the same velocity as the gravity current front.

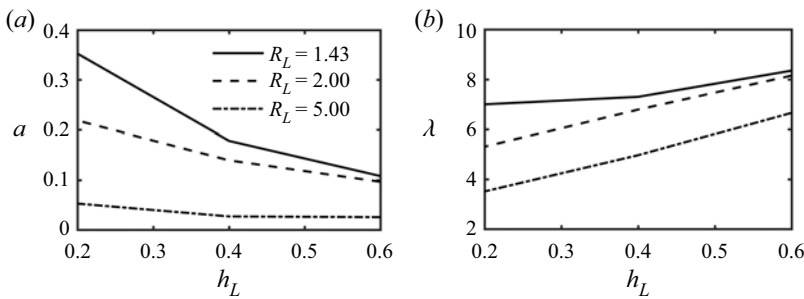


Figure 15. The dependence of (a) the amplitude  $a$ , and (b) the wavelength  $\lambda$  of the undular bore waves, on  $h_L$  and  $R_L$ .

### 3.3.2. Amplitude and wavelength of the undular bore waves

We take half of the average vertical distance between adjacent crests and troughs as the amplitude  $a$ , and twice the average horizontal distance as the wavelength  $\lambda$ . Figure 15(a) shows that the amplitude  $a$  decreases with larger  $h_L$  and  $R_L$ . Figure 15(b) indicates that the wavelength  $\lambda$  increases with larger  $h_L$  and decreases with higher  $R_L$ .

### 3.4. Vorticity-based model

Above, we calculated  $h_{ep}$ ,  $U_w$  and  $U_f$  based on the computational observation that the gravity current behaves approximately as a half-depth current with  $h_{gc} \approx 1$ , and by using the empirical assumption of hydrostatic pressure balance  $p_1 = p_2$ . In the following, we will employ the conservation of mass and vorticity to develop a more comprehensive, self-contained and closed model that does not require such empirical assumptions. The derivation of this model builds on the earlier work by Khodkar *et al.* (2016).

Figure 16 illustrates the flow field under consideration. After removal of the gate, the lock fluid forms a right-propagating gravity current of undetermined height  $\hat{h}_{gc}$  that propagates with velocity  $\hat{U}_f$ . Simultaneously, a left-propagating buoyant gravity current

Removal of a dense bottom layer by a gravity current

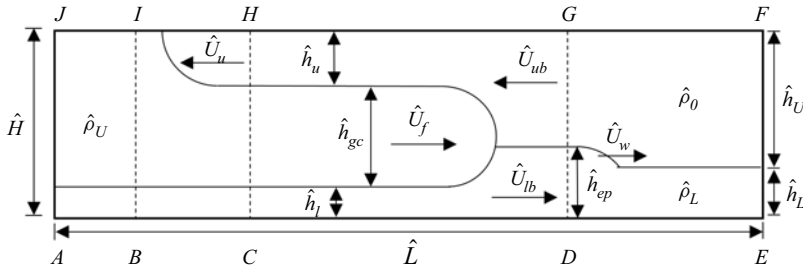


Figure 16. Schematic of a gravity current interacting with the bottom fluid layer, for developing the vorticity-based model described in the text.

with density  $\hat{\rho}_0$  and height  $\hat{h}_u$  emerges along the top wall. Ahead of the gravity current, a bore of thickness  $\hat{h}_{ep}$  propagates along the interface with velocity  $\hat{U}_w$ . Behind the bore front, the upper and lower layers have velocities  $\hat{U}_{ub}$  and  $\hat{U}_{lb}$ , respectively. The flow is fully described by nine unknowns:  $\hat{U}_f$ ,  $\hat{U}_u$ ,  $\hat{U}_w$ ,  $\hat{U}_{ub}$ ,  $\hat{U}_{lb}$ ,  $\hat{h}_l$ ,  $\hat{h}_u$ ,  $\hat{h}_{gc}$  and  $\hat{h}_{ep}$ , as shown in figure 16.

Within control volume  $DEFG$ , and in the reference frame moving with the bore, mass conservation for the upper and lower layers, along with vorticity conservation along the interface give

$$\hat{U}_w \hat{h}_L = (\hat{U}_w - \hat{U}_{lb}) \hat{h}_{ep}, \quad (3.10)$$

$$\hat{U}_w \hat{h}_U = (\hat{U}_w + \hat{U}_{ub}) (\hat{H} - \hat{h}_{ep}), \quad (3.11)$$

$$\hat{g}'_L (\hat{h}_{ep} - \hat{h}_L) = \left( \hat{U}_w + \frac{\hat{U}_{ub} - \hat{U}_{lb}}{2} \right) (\hat{U}_{lb} + \hat{U}_{ub}), \quad (3.12)$$

where  $\hat{g}'_L = \hat{g}(\hat{\rho}_L - \hat{\rho}_0)/\hat{\rho}_0$ .

In control volume  $CDGH$ , in the reference frame moving with the intrusion, the two continuity equations for the upper and lower layers can be written as

$$(\hat{U}_f - \hat{U}_{lb}) \hat{h}_{ep} = \hat{U}_f \hat{h}_l, \quad (3.13)$$

$$(\hat{U}_f + \hat{U}_{ub}) (\hat{H} - \hat{h}_{ep}) = (\hat{U}_f + \hat{U}_u) \hat{h}_u. \quad (3.14)$$

The vorticity conservation equations along the respective interfacial segments are

$$-(\hat{g}'_L - \hat{g}'_U) (\hat{h}_{ep} - \hat{h}_l) + \frac{\hat{g}'_L - \hat{g}'_U}{\hat{g}'_L} \left( \hat{U}_f + \frac{\hat{U}_{ub} - \hat{U}_{lb}}{2} \right) (\hat{U}_{ub} + \hat{U}_{lb}) = -\frac{1}{2} \hat{U}_f^2, \quad (3.15)$$

$$\hat{g}'_U (\hat{H} - \hat{h}_{ep} - \hat{h}_u) + \frac{\hat{g}'_U}{\hat{g}'_L} \left( \hat{U}_f + \frac{\hat{U}_{ub} - \hat{U}_{lb}}{2} \right) (\hat{U}_{ub} + \hat{U}_{lb}) = \frac{1}{2} (\hat{U}_u + \hat{U}_f)^2, \quad (3.16)$$

where  $\hat{g}'_U = \hat{g}(\hat{\rho}_U - \hat{\rho}_0)/\hat{\rho}_0$ . In addition, we have the geometrical constraint

$$\hat{h}_{gc} + \hat{h}_u + \hat{h}_l = \hat{H}. \quad (3.17)$$

For control volume  $BCHI$ , in the frame moving with the upper gravity current front, the vorticity conservation yields

$$\hat{g}'_U \hat{h}_u = \frac{1}{2} (\hat{U}_u + \hat{U}_f)^2. \quad (3.18)$$

After non-dimensionalization, we obtain the following system of eight coupled, nonlinear equations:

$$U_w h_L = (U_w - U_{lb}) h_{ep}, \tag{3.19}$$

$$U_w h_U = (U_w + U_{ub})(H - h_{ep}), \tag{3.20}$$

$$R_L(h_{ep} - h_L) = \left( U_w + \frac{U_{ub} - U_{lb}}{2} \right) (U_{lb} + U_{ub}), \tag{3.21}$$

$$(U_f - U_{lb}) h_{ep} = U_f h_l, \tag{3.22}$$

$$(U_f + U_{ub})(H - h_{ep}) = (U_f + U_u) h_u, \tag{3.23}$$

$$(1 - R_L)(h_{ep} - h_l) + \frac{R_L - 1}{R_L} \left( U_f + \frac{U_{ub} - U_{lb}}{2} \right) (U_{ub} + U_{lb}) = -\frac{1}{2} U_f^2, \tag{3.24}$$

$$H - h_{ep} - h_u + \frac{1}{R_L} \left( U_f + \frac{U_{ub} - U_{lb}}{2} \right) (U_{ub} + U_{lb}) = \frac{1}{2} (U_u + U_f)^2, \tag{3.25}$$

$$h_u = \frac{1}{2} (U_u + U_f)^2. \tag{3.26}$$

Note that we have already eliminated  $\hat{h}_{gc}$  by making use of the geometrical constraint. This system can be solved efficiently with the MATLAB function `vpsolve`.

Figure 17(a) shows values of the gravity current height  $h_{gc}$  predicted by the model, as a function of  $R_L$  and  $h_L$ , along with the corresponding simulation results. Here the gravity current height for the simulation is obtained by time-averaging over  $10 < t < 25$  the quantity

$$h_{gc} = \int_{h_U - H}^{h_U} s_U dy \tag{3.27}$$

at the gate location  $x = 10$ . The simulation results are generally within approximately 10 % of the vorticity model predictions. Especially for smaller values of  $R_L$ , the predicted and simulated intrusion heights are substantially larger than the value  $h_{gc} = 1$  that we had assumed for the earlier empirical model that resulted in (3.9), which highlights the limitations of that model. For  $h_L > 0.2$ , the predicted intrusion thickness  $h_{gc}$  varies only weakly with  $h_L$ .

Figure 17(b) shows predictions by the vorticity model for the equilibrium height  $h_{ep}$ , which is seen to vary approximately linearly with the height of the bottom fluid layer  $h_L$ . For  $R_L < 3$ ,  $h_{ep}$  decreases rapidly as  $R_L$  grows, which reflects the fact that denser bottom layers are less easily removed by gravity currents. The predictions by the vorticity models generally lie within approximately 10 % of the simulation data.

Vorticity model predictions for the bore velocity  $U_w$  are presented in figure 17(c). Just as we had seen for the other flow variables, the predictions are reasonably close to the corresponding simulation data, and they show that  $U_w$  increases with  $h_L$  and  $R_L$ , consistent with the shallow water wave speed given by (3.5).

### 3.5. Energy budget

In applications where a dense bottom layer is to be removed by means of employing a gravity current, the only source of energy that we have available for dislodging the dense fluid is the potential energy initially contained in the gravity current fluid. This energy then needs to be transferred to the dense bottom layer in order to dislodge it. Hence, it



Removal of a dense bottom layer by a gravity current

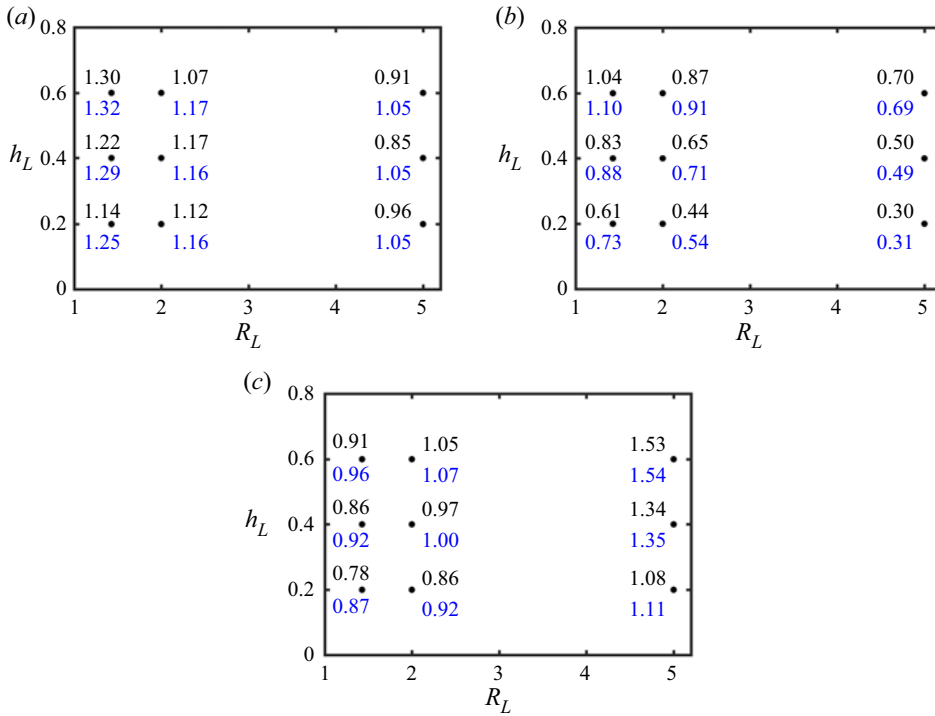


Figure 17. The dependence of (a)  $h_{gc}$ , (b)  $h_{ep}$  and (c)  $U_w$  on  $R_L$  and  $h_L$ . The black and blue numbers indicate simulation results and values predicted by the model, respectively.

is of interest to study how efficiently the potential energy of the gravity current fluid is converted into potential and kinetic energy of the dense bottom fluid. Towards this end, we define the potential energy  $E_p$ , kinetic energy  $E_k$  and dissipated energy  $E_d$  of the flow, respectively, as

$$E_p(t) = \int_{h_U-H}^{h_U} \int_0^L (s_U + R_L s_L) y \, dx \, dy, \quad (3.28)$$

$$E_k(t) = \int_{h_U-H}^{h_U} \int_0^L \frac{1}{2} (u^2 + v^2) \, dx \, dy, \quad (3.29)$$

$$E_d(t) = \int_0^t \varepsilon(\tau) \, d\tau. \quad (3.30)$$

Note that the potential energy is evaluated relative to a situation with ambient fluid everywhere, and relative to the initial lower boundary of the gravity current and ambient fluids at  $y = 0$ . Here  $\varepsilon$  indicates the instantaneous viscous dissipation rate

$$\varepsilon(t) = \int_{h_U-H}^{h_U} \int_0^L \frac{2}{Re} s_{ij} s_{ij} \, dx \, dy, \quad (3.31)$$

with  $s_{ij}$  denoting the rate-of-strain tensor

$$s_{ij} = \frac{1}{2} \left( \frac{\partial u_i}{\partial x_j} + \frac{\partial u_j}{\partial x_i} \right). \quad (3.32)$$

Since the fluid is at rest initially, the overall energy budget of the flow thus takes the form

$$E_{total} = E_p + E_k + E_d = \text{const.} = E_{p,init} \quad (3.33)$$

where  $E_{p,init}$  represents the initial potential energy. In order to investigate the time-dependent exchange of potential and kinetic energy, and the energy transfer from the gravity current to the dense lower layer and to the ambient fluid, we consider their respective contributions to the overall energy budget

$$E_k = E_{kU} + E_{kL} + E_{k0}, \quad (3.34)$$

$$E_p = E_{pU} + E_{pL}, \quad (3.35)$$

$$E_d = E_{dU} + E_{dL} + E_{d0}, \quad (3.36)$$

$$\varepsilon = \varepsilon_U + \varepsilon_L + \varepsilon_0, \quad (3.37)$$

where the subscripts  $U, L$  and  $0$  again refer to gravity current, dense fluid layer and ambient fluid, respectively. These contributions take the form

$$E_{kU}(t) = \int_{h_U-H}^{h_U} \int_0^L s_U \frac{1}{2} (u^2 + v^2) \, dx \, dy, \quad (3.38)$$

$$E_{kL}(t) = \int_{h_U-H}^{h_U} \int_0^L s_L \frac{1}{2} (u^2 + v^2) \, dx \, dy, \quad (3.39)$$

$$E_{k0}(t) = \int_{h_U-H}^{h_U} \int_0^L (1 - s_U - s_L) \frac{1}{2} (u^2 + v^2) \, dx \, dy, \quad (3.40)$$

$$E_{pU}(t) = \int_{h_U-H}^{h_U} \int_0^L s_U y \, dx \, dy, \quad (3.41)$$

$$E_{pL}(t) = \int_{h_U-H}^{h_U} \int_0^L R_L s_L y \, dx \, dy, \quad (3.42)$$

$$\varepsilon_U(t) = \int_{h_U-H}^{h_U} \int_0^L s_U \frac{2}{Re} s_{ij} s_{ij} \, dx \, dy, \quad (3.43)$$

$$\varepsilon_L(t) = \int_{h_U-H}^{h_U} \int_0^L s_L \frac{2}{Re} s_{ij} s_{ij} \, dx \, dy, \quad (3.44)$$

$$\varepsilon_0(t) = \int_{h_U-H}^{h_U} \int_0^L (1 - s_U - s_L) \frac{2}{Re} s_{ij} s_{ij} \, dx \, dy. \quad (3.45)$$

As a representative example, [figure 18](#) shows the time history of all energy components for run 2, cf. [figure 5](#). Each component is normalized by the initial potential energy of the gravity current fluid  $E_{pU,init}$ . The total energy  $E_{total}$  is seen to vary by less than 2% over the course of the simulation, which reflects the good energy conservation properties of the simulation code. Over the first 15 time units,  $E_{pU}$  rapidly decreases by approximately 50%, as the intermediate density lock fluid collapses and forms the gravity current. This potential energy is converted in approximately equal parts to kinetic energy of the gravity current and ambient fluids. Since we evaluate the potential energy relative to  $y = 0$ , its

## Removal of a dense bottom layer by a gravity current

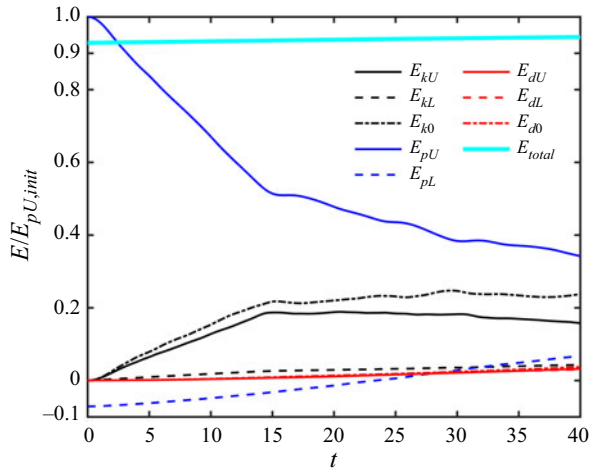


Figure 18. Time history of the various energy budget components for run 2, with  $R_L = 1.43$  and  $h_L = 0.2$ . The potential energy given up by the gravity current fluid is converted in nearly equal parts to kinetic energy of the gravity current and ambient fluids, with smaller contributions going towards raising the potential energy of the dense fluid layer, and to dissipation.

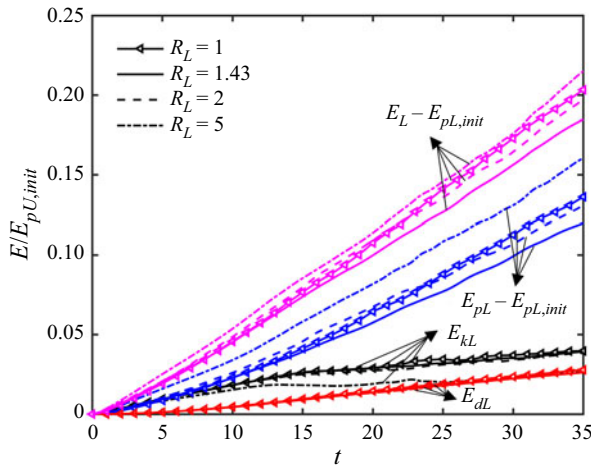


Figure 19. Time history of the dense layer energy budget components for runs 1, 2, 3 and 4 with  $R_L = 1, 1.43, 2$  and  $5$  and  $h_L = 0.2$ . While the potential energy of the dense layer grows more rapidly for larger  $R_L$  (blue lines) (except  $R_L = 1$ ), its kinetic energy grows more slowly (black lines).

initial value for the dense fluid layer is negative. However, as the dense fluid is eroded by the gravity current and forms the high-amplitude interfacial wave seen in figure 5, its potential and kinetic energies gradually increase. All three dissipated energy components  $E_{dU}$ ,  $E_{d0}$  and  $E_{dL}$  remain relatively small throughout the simulation.

Figure 19 shows the influence of the density ratio  $R_L$  on the evolution of the individual energy budget components of the dense fluid layer. When  $R_L = 1$ , the bottom layer has the same density as the gravity current, so that it can easily be eroded and uplifted, thereby gaining potential energy. Initially, as  $R_L$  increases the potential energy gain of the lower layer decreases, as it becomes harder to lift up the dense layer fluid. Beyond  $R_L = 1.43$ , however, the uplifted fluid contains more potential energy for larger  $R_L$  even though

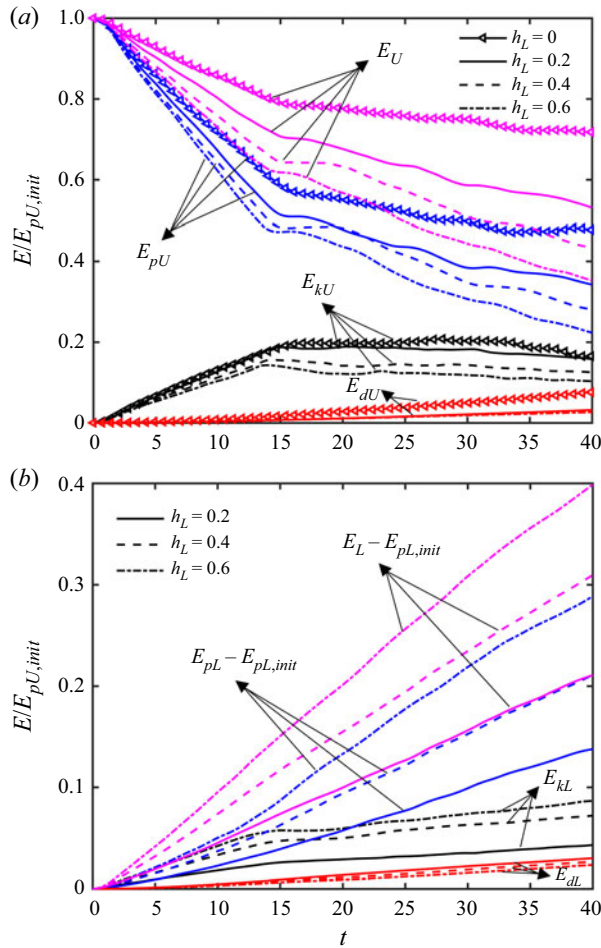


Figure 20. Time history of the various energy budget components in runs 2, 5 and 8 with  $h_L = 0.2, 0.4$  and  $0.6$ , and  $R_L = 1.43$ , together with run 11 for  $h_L = 0$ . (a) Gravity current fluid: since the gravity current fluid sinks more deeply into thicker bottom layers, it loses its potential energy more rapidly (blue lines), while its kinetic energy increases more slowly (black lines), so that its overall energy decreases for larger  $h_L$  (magenta lines). (b) Dense layer fluid: as the gravity current fluid penetrates thicker bottom layers more deeply, the dense fluid is being lifted up more strongly, so that its potential energy increases more rapidly (blue lines), as does its kinetic energy (black lines).

the wave amplitude continues to decrease, due to its higher density. The high-amplitude internal waves for small  $R_L$  contain more kinetic energy than the low-amplitude waves for large  $R_L$ , so that  $E_{kL}$  decreases with increasing  $R_L$ . The amount of energy dissipated by the lower layer does not show a strong dependence on  $R_L$ .

Figure 20 analyses the influence of the dense fluid layer thickness  $h_L$  on the energy conversion and transfer processes. Figure 20(a) shows the evolution of the energy components in the gravity current fluid. For larger  $h_L$ -values, the gravity current fluid sinks more deeply into the dense fluid layer, cf. figure 7, so that it loses its potential energy  $E_{pU}$  more rapidly, while its kinetic energy  $E_{kU}$  increases more slowly. Consistent with this slower kinetic energy increase for larger  $h_L$ , the dissipated energy  $E_{dU}$  is smallest for the deepest dense fluid layer.

The time history of the various energy components for the dense fluid layer as a function of  $h_L$  is shown in [figure 20\(b\)](#). As we saw above, the gravity current sinks more deeply into the dense layer when this is thicker. As a result, more of the dense fluid is being lifted up, so that the potential energy gain of the bottom fluid layer increases for larger  $h_L$ -values. While the internal waves have a smaller amplitude for larger  $h_L$ , their velocity is higher, so that the dense fluid layer acquires more kinetic energy. In summary, thicker dense fluid layers see a more rapid increase in their overall energy.

#### 4. Conclusions

We have explored the removal of a dense fluid layer above a horizontal bottom wall by a lock-release gravity current, via 2-D Navier–Stokes simulations in the Boussinesq limit. As the two dominant dimensionless quantities governing this problem, we identify a thickness parameter for the dense bottom layer, and the density ratio given by the differences between the densities of the bottom layer, the gravity current and the ambient fluid. After releasing the lock fluid, we observe the formation of a quasisteady gravity current which displaces some of the dense bottom layer fluid, so that it accumulates ahead of the gravity current and forms an undular bore or a series of internal gravity waves. These propagate ahead of the current, along the interface between the dense fluid layer and the ambient fluid. Depending on the ratio of the gravity current front velocity and the linear shallow-water wave velocity of interfacial waves, we observe the existence of different flow regimes. If the linear wave velocity is larger than the gravity current velocity, the waves quickly move ahead of, and away from, the gravity current front, and their amplitude remains small. On the other hand, when the linear wave velocity is comparable to or smaller than the gravity current velocity, the waves steepen and a train of nonlinear internal waves form whose amplitude can be comparable to the thickness of the gravity current.

The simulations indicate that the gravity current behaves similarly to a half-depth current whose front velocity can be estimated from the models of Benjamin (1968) and Borden & Meiburg (2013a). In addition, the propagation velocity of the undular bore or the train of nonlinear waves can be obtained from the vorticity model of Borden & Meiburg (2013b), after defining an equilibrium layer thickness by averaging the interface height over the individual waves. With these approximations, and with the empirical assumption that the hydrostatic pressures at the bottom wall below the gravity current front and ahead of it are in balance, we can set up a semiempirical model for predicting the rate at which dense fluid is being eroded by the gravity current.

Furthermore, we develop a more sophisticated model that does not require the above empirical assumptions, based on the conservation principles for mass and vorticity. This model is able to predict such quantities as the gravity current height, the equilibrium layer thickness and the internal wave velocity as a function of the dimensionless parameters, generally to within approximately a 10 % accuracy.

Finally, an energy budget analysis provides information on the rates at which potential energy is converted into kinetic energy and dissipated, and on the processes by which it is transferred from the gravity current fluid to the dense layer and the ambient fluids. Both the numerical simulations and the vorticity model indicate that the gravity current sinks more deeply into thicker bottom layers, which accelerates the transfer of energy from the gravity current to the dense fluid layer. In addition, for situations with equal bottom layer thicknesses, the energy of the denser bottom layer grows more rapidly.

**Funding.** Funding for this work was provided under NSF grant CBET-1936358. Computational resources for this work used the Extreme Science and Engineering Discovery Environment (XSEDE), which was supported by the National Science Foundation, USA, grant no. TG-CTS150053. R.Z. thanks The National Natural Science

Foundation of China (11672267) and the China Scholarship Council for providing him with a scholarship to study at UCSB.

**Declaration of interests.** The authors report no conflict of interest.

**Author ORCID.**

 Zhiguo He <https://orcid.org/0000-0002-0612-9062>;

 Eckart Meiburg <https://orcid.org/0000-0003-3670-8193>.

REFERENCES

- BENJAMIN, T.B. 1968 Gravity currents and related phenomena. *J. Fluid Mech.* **31** (2), 209–248.
- BIEGERT, E., VOWINCKEL, B. & MEIBURG, E. 2017*a* A collision model for grain-resolving simulations of flows over dense, mobile, polydisperse granular sediment beds. *J. Comput. Phys.* **340**, 105–127.
- BIEGERT, E., VOWINCKEL, B., OUILLOIN, R. & MEIBURG, E. 2017*b* High-resolution simulations of turbidity currents. *Prog. Earth Planet. Sci.* **4** (1), 33.
- BORDEN, Z. & MEIBURG, E. 2013*a* Circulation based models for Boussinesq gravity currents. *Phys. Fluids* **25** (10), 101301.
- BORDEN, Z. & MEIBURG, E. 2013*b* Circulation-based models for Boussinesq internal bores. *J. Fluid Mech.* **726**, R1.
- BRITTER, R.E. & SIMPSON, J.E. 1981 A note on the structure of the head of an intrusive gravity current. *J. Fluid Mech.* **112**, 459–466.
- CARVALHO, L., *et al.* 2020 The sundowner winds experiment (SWEX) pilot study: understanding downslope windstorms in the Santa Ynez Mountains, Santa Barbara, California. *Mon. Weather Rev.* **148** (4), 1519–1539.
- CHEONG, H.-B., KUENEN, J.J.P. & LINDEN, P.F. 2006 The front speed of intrusive gravity currents. *J. Fluid Mech.* **552**, 1–11.
- DE ROOIJ, F., LINDEN, P.F. & DALZIEL, S.B. 1999 Saline and particle-driven interfacial intrusions. *J. Fluid Mech.* **389**, 303–334.
- FLYNN, M.R. & LINDEN, P.F. 2006 Intrusive gravity currents. *J. Fluid Mech.* **568**, 193–202.
- HE, Z., ZHAO, L., LIN, T., HU, P., LV, Y., HO, H.-C. & LIN, Y.-T. 2017 Hydrodynamics of gravity currents down a ramp in linearly stratified environments. *J. Hydraul. Engng* **143** (3), 04016085.
- HE, Z., ZHAO, L., ZHU, R. & HU, P. 2019 Separation of particle-laden gravity currents down a slope in linearly stratified environments. *Phys. Fluids* **31** (10), 106602.
- HOLYER, J.Y. & HUPPERT, H.E. 1980 Gravity currents entering a two-layer fluid. *J. Fluid Mech.* **100** (4), 739–767.
- KHODKAR, M.A., NASR-AZADANI, M.M. & MEIBURG, E. 2016 Intrusive gravity currents propagating into two-layer stratified ambients: vorticity modeling. *Phys. Rev. Fluid* **1** (4), 044302.
- KUNDU, P.K. & COHEN, I.M. 2001 *Fluid Mechanics*, pp. 214–277. Elsevier.
- LATTEMANN, S. & AMY, G. 2013 Marine monitoring surveys for desalination plants—a critical review. *Desalination Water Treat.* **51** (1–3), 233–245.
- LOWE, R.J., LINDEN, P.F. & ROTTMAN, J.W. 2002 A laboratory study of the velocity structure in an intrusive gravity current. *J. Fluid Mech.* **456**, 33–48.
- MEHTA, A.P., SUTHERLAND, B.R. & KYBA, P.J. 2002 Interfacial gravity currents. II. Wave excitation. *Phys. Fluids* **14** (10), 3558–3569.
- MONAGHAN, J.J. 2007 Gravity current interaction with interfaces. *Annu. Rev. Fluid Mech.* **39**, 245–261.
- NASR-AZADANI, M.M., HALL, B. & MEIBURG, E. 2013 Polydisperse turbidity currents propagating over complex topography: comparison of experimental and depth-resolved simulation results. *Comput. Geosci.* **53**, 141–153.
- NASR-AZADANI, M.M. & MEIBURG, E. 2011 Turbines: an immersed boundary, Navier–Stokes code for the simulation of gravity and turbidity currents interacting with complex topographies. *Comput. Fluids* **45** (1), 14–28.
- NECKER, F., HÄRTEL, C., KLEISER, L. & MEIBURG, E. 2005 Mixing and dissipation in particle-driven gravity currents. *J. Fluid Mech.* **545**, 339–372.
- OOI, S.K., CONSTANTINESCU, G. & WEBER, L.J. 2007 2D large-eddy simulation of lock-exchange gravity current flows at high Grashof numbers. *J. Hydraul. Eng.* **133** (9), 1037–1047.
- OUILLOIN, R., MEIBURG, E., OUELLETTE, N.T. & KOSEFF, J.R. 2019*a* Interaction of a downslope gravity current with an internal wave. *J. Fluid Mech.* **873**, 889–913.

## *Removal of a dense bottom layer by a gravity current*

- OUILLO, R., MEIBURG, E. & SUTHERLAND, B.R. 2019*b* Turbidity currents propagating down a slope into a stratified saline ambient fluid. *Environ. Fluid Mech.* **19** (5), 1143–1166.
- SAMOTHRAKIS, P. & COTEL, A.J. 2006*a* Finite volume gravity currents impinging on a stratified interface. *Exp. Fluids* **41** (6), 991–1003.
- SAMOTHRAKIS, P. & COTEL, A.J. 2006*b* Propagation of a gravity current in a two-layer stratified environment. *J. Geophys. Res.-Oceans* **111**, C01012.
- SIMPSON, J.E. 1982 Gravity currents in the laboratory, atmosphere, and ocean. *Annu. Rev. Fluid Mech.* **14** (1), 213–234.
- SMITH, C., HATCHETT, B. & KAPLAN, M. 2018 Characteristics of sundowner winds near Santa Barbara, CA, from a dynamically downscaled climatology: environment and effects aloft and offshore. *J. Geophys. Res.-Atmos.* **123** (23), 13–092.
- SUTHERLAND, B.R., KYBA, P.J. & FLYNN, M.R. 2004 Intrusive gravity currents in two-layer fluids. *J. Fluid Mech.* **514**, 327–353.
- TANIMOTO, Y., OUELLETTE, N.T. & KOSEFF, J.R. 2020 Interaction between an inclined gravity current and a pycnocline in a two-layer stratification. *J. Fluid Mech.* **887**, A8.